J Mater Sci (2011) 46:4420–4427
DOI 10.1007/s10853-010-5242-5

IIB 2010

Plasticity of an alumina bicrystal near the rhombohedral twin orientation

Shehrazed Moulahem · Sylvie Lartigue-Korinek · Jacques Castaing

Received: 31 August 2010 / Accepted: 30 December 2010 / Published online: 15 January 2011

Abstract A bicrystal slightly deviated from the rhombohedral twin orientation is deformed by creep so as to activate two basal slip systems in each grain. The tilt deviation in the starting bicrystal is accommodated by two parallel arrays of disconnections with the smallest twin Burgers vectors and large associated steps. Dislocations from both grains interact with the grain boundary (GB) and the tilt deviation increases by 3.6°, giving rise to an array of pure edge disconnections with no associated steps. Interfacial defects are interpreted by reactions between incoming dislocations and GB disconnections. Decompositions of dislocations into GB disconnections are followed by glide and climb of products that can annihilate or interact to give a perfect wall of edge disconnections superimposed to the twin boundary perfect structure. Owing to their large Burgers vectors, the final disconnections are always dissociated.

Introduction

Grain boundary (GB) dislocations play a major role in high temperature deformation of polycrystalline alumina with small grain size and no intergranular glassy phase. In fine-grained Mg–alumina, the main deformation process is GB sliding, which involves GB dislocation glide and climb, processes that are controlled by GB diffusion [1, 2]. In polycrystals, obstacles to GB sliding create local stress concentrations that may be relieved by emission of lattice dislocations that interact with opposite GBs. Thus, GB dislocations generally result from the interaction of lattice dislocations with GBs or may be created directly in the GBs [3, 4]. Both GB sliding and dislocation accommodation processes depend on the structure and chemistry of GBs. Alumina creep properties may be strongly modified by addition of dopants that most often present a low solubility limit and are thus segregated to GBs; for example, yttrium reduces creep rate [5–7]. Direct evidence for yttrium segregation on intergranular dislocation cores was emphasized in bicrystals with the rhombohedral twin orientation [8]. In fine-grained Y-doped alumina polycrystals, the presence of numerous defects in most GBs after creep strongly supports the role of dislocations during creep. The reduced creep rate may be interpreted by a decrease in dislocation mobility induced by yttrium segregation [2, 7].

The role of GB characteristics on sliding has been directly investigated on bicrystals both in ceramic and metallic materials.

A distinction has to be made between "pure" GB sliding where no intragranular slip occurs and GB sliding which involves interactions between lattice dislocations and GBs.

Pure GB sliding

In copper, low energy GBs show less resistance to sliding [9]. In alumina tilt bicrystals, the highest resistance to sliding occurs in GBs with the largest atomic density at their cores [10]. The role of segregation in sliding is emphasized on tilt bicrystals in alumina undoped or doped

S. Moulahem · S. Lartigue-Korinek (✉)
Institut de Chimie et des Matériaux Paris-Est, UMR 7182 CNRS et Université Paris 12, 2-8 rue H. Dunant, 94320 Thiais, France
e-mail: sylvie.lartigue@icmpe.cnrs.fr

J. Castaing
C2RMF, CNRS UMR 171, Palais du Louvre, 14 quai François Mitterrand, 75001 Paris, France

Present Address:
S. Moulahem
LMDM, Université de Mentouri, Constantine, Algeria

with yttrium: The GB sliding rate is decreased by two orders of magnitude with yttrium addition [11]. This effect is interpreted by an increase in ionicity of Al–O bonds found from ab initio calculations [12]. Other calculations show that segregation of large cations result in a large increase in the GB sliding barrier due to the change in the Al–O bonding at the GB core [13, 14]. However, experimental sliding behaviour may be due to diffusional accommodation; dislocations sources directly emitted in the GBs may also play a role in sliding. [15, 16].

GB sliding and intragranular slip

There is extensive evidence that GB sliding is enhanced when the adjoining crystals undergo slip. In zinc bicrystals, sliding is drastically increased when lattice dislocations interact with the GB [17–19]. GB sliding due to the motion of GB dislocations introduced by decomposition of lattice dislocations is also observed in ceramics [20].

Thus, the absorption of lattice dislocations appears as an important elementary process.

The overall objective of our work on doped bicrystals is to emphasize the mechanisms of interaction between lattice dislocations and GBs, in particular, the accommodation processes in relation with the bicrystal chemistry. The applied stress is nearly perpendicular to the GB, so the bicrystal should not exhibit GB sliding.

This article presents the first results obtained on a bicrystal codoped with magnesium and yttrium as it was the case for our previous polycrystalline fine-grained samples. Magnesium has a low solubility in alumina [21] and is segregated to GBs; its benefit role in promoting an equiaxed microstructure is complex. Co-doping of magnesium and silicon increases their mutual bulk solubilities, thus impeding the formation of silicon rich glassy phase at the GB and reducing GB mobility [22, 23]. Magnesium also increases and homogenizes GB diffusion [24].

Work is in progress on the respective behaviour of bicrystals doped with other elements; the role of GB segregation in creep is beyond the scope of this article, merely focussed on the GB defect crystallography.

The bicrystals are deformed by compression. Before describing the creep experiments and transmission electron microscopy (TEM) methods, the chosen orientation of bicrystals in relation with the alumina plasticity behaviour is presented. The Result and discussion section describes the structural defects of the initial bicrystal. The main deformation microstructural features are then analysed. Conventional and high-resolution TEM (HRTEM) investigations allow us to propose GB deformation micromechanisms in relation with the macroscopic deformation behaviour.

Crystallographic parameters of bicrystals and creep deformation

Plastic deformation of single-crystal Al_2O_3 has been of interest for many years [25–31]. The two main slip systems are basal slip $(0001)1/3\langle 2\bar{1}\bar{1}0\rangle$ (Fig. 1), and prism plane slip $\{11\bar{2}0\}\langle 10\bar{1}0\rangle$. Basal slip has the lowest critical resolved shear stress at all temperatures above 700 °C, although prism plane slip is preferred at low temperature [28]. The temperature dependence of the CRSS for the two systems has been recently interpreted on the basis of dislocation glide controlled by a Peierls mechanism [29]. A temperature of 1400 °C has been chosen for the experiments on bicrystals. It is sufficiently high to promote GB/dislocations interactions without the help of a hydrostatic pressure, and it is sufficiently low to avoid a damage of rams in the creep machine. Thus, basal slip should be activated in our samples. However, for most orientations, rhombohedral twinning can also occur, a shear stress of 15 MPa being sufficient to propagate a twin whatever the temperature [30]. It is recalled that the GB is a rhombohedral twin described by a common dense $(01\bar{1}2)$ plane and a common $[01\bar{1}\bar{1}]$ direction in the GB plane. The other direction contained in the GB plane and perpendicular to $[01\bar{1}\bar{1}]$ is $[2\bar{1}\bar{1}0]$ in one crystal parallel to $[\bar{2}110]$ in the other crystal. Taking into account the small size of our bicrystals, the applied stress could only be applied in a direction perpendicular to one of the three sample faces: $[2\bar{1}\bar{1}0]$, $[01\bar{1}\bar{1}]$ and the irrational direction normal to the GB plane $(01\bar{1}2)$. The only direction for the applied stress that avoids twinning is the normal to the GB plane [31].

In this orientation, two basal slip systems have the same Schmid factor for this orientation (Fig. 2), the basal planes have a common trace in the GB plane (angle of 57.6° with the GB plane), and the Burgers vectors make an angle of ±30° with the normal to the GB: $\vec{b}_\lambda = \frac{1}{3}[11\bar{2}0]$, or $\vec{b}_\lambda = \frac{1}{3}[\bar{1}2\bar{1}0]$, in the upper crystal λ, $\vec{b}_\mu = \frac{1}{3}[\bar{1}\bar{1}20]$, or $\vec{b}_\mu = \frac{1}{3}[1\bar{2}10]$ in the lower crystal μ.

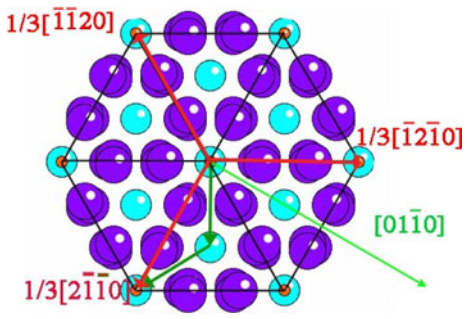

Fig. 1 Schema of perfect basal dislocations $^1/_3\langle 2\bar{1}\bar{1}0\rangle$ in the basal plane. The prism plane dislocation $[01\bar{1}0]$ is also shown. (*Large circles*: O, *small circles*: Al)

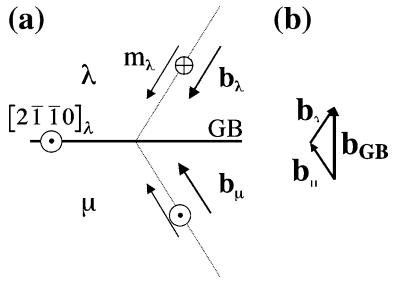

Fig. 2 Symmetrical glide in a bicrystal. **a** Symmetrical movement of dislocations. The glide directions in the basal planes (*dotted lines*) are opposite. The Burgers vectors are inclined (±30°) on the projection. ($\vec{b}_\lambda = 1/3[11\bar{2}0]$ up, or $\vec{b}_\lambda = 1/3[\bar{1}2\bar{1}0]$ down, $\vec{b}_\mu = 1/3[\bar{1}\bar{1}20]$ up, or $\vec{b}_\mu = 1/3[1\bar{2}10]$ down). **b** Burgers vectors balance at the GB

Materials and methods

Bicrystals have been fabricated by diffusion bonding at the Institute of Crystallography in Moscow. Doping elements are deposited on single-crystal surface by pulsed laser deposition. Joining is carried out at 1700 °C during 30 nm under an applied stress of 50 MPa. [32]. Specimens for creep experiments with dimensions of 2.5 × 2.5 × 5 mm^3 were carefully polished with a tripod. Compressive tests were carried out in air environment at a temperature of 1400 °C with stress varying up to 50 MPa. Compression rams were made of sintered alumina bars coupled with sapphire rods oriented along the *c*-axis. Temperature was measured with two sets of B-type thermocouples located in the furnace in the near vicinity of the specimens. Strains during the creep tests were calculated from the displacements of the ram ends measured using a linear transducer. The first sample has been deformed up to 0.13%. Foil thinning has been described previously [8].

Classical HRTEM images were recorded along the $[2\bar{1}\bar{1}0]_1//[\bar{2}110]_2$ zone axis with a Topcon ABT002 operated at 200 kV that exhibits a Scherzer point resolution of 1.8 Å.

The main structural parameters of the disconnections have been determined on the HRTEM images by fitting models based on the lattice sites of the alumina structure. The dislocation Burgers vectors and step heights are deduced from a circuit around the defect mapped in the dichromatic pattern of the twin [33]. The structural models are built using the Crystal Kit software written by Kilaas [34].

Conventional 2-beam diffraction contrast analyses were performed on a JEOL 2000EX (200 kV, W filament). The basal plane is edge-on for the thin foil orientation, so the determination of the lattice dislocations Burgers vectors was challenging. A method based on the analysis of the contrast symmetry has been used [35].

Results and discussion

Bicrystal before deformation

Undoped and doped α-alumina bicrystals with the rhombohedral twin orientation present a same arrangement of two periodic arrays of parallel dislocations with different Burgers vectors that account for the tilt deviation (0.8°) from the perfect twin orientation. No dislocation occurs inside the grains. The defect distribution of the bicrystal is shown in Fig. 3. The perfect twin structure is accurately established [36–40]. It is centred on empty sites of alumina and presents a 2-fold symmetry axis with a glide (screw twin [36]) at the interface.

According to the topological approach [33], these defects are merely defined as disconnections as they present both a "step and dislocation" character. The two disconnections have a mixed (screw/edge) dislocation character; in part A of Fig. 3, adjacent defects exhibit screw components of opposite sign to cancel stress fields [41]. Extrinsic dislocations are also seen, so the GB is not in perfect equilibrium state. Figure 4 shows a HRTEM image of four disconnections with various Burgers vectors.

Figure 5 presents the bright field image of one disconnection [type (a) in Fig. 4)]. The twin plane is lower on the right side of the disconnection. The Burgers vector is identified as $\vec{b}_{-3/-4}$. According to the terminology defined in [42], the notation adopted for the Burgers vector is $b_{p/q}$, where p and q denote the step heights in units of the spacing d of the $(01\bar{1}2)$ lattice planes in the upper and the lower crystal. In Fig. 5, the disconnection steps down from the left to the right and the step is three planes height in the upper crystal and four planes height in the lower crystal. The Burgers vector has a component perpendicular to the

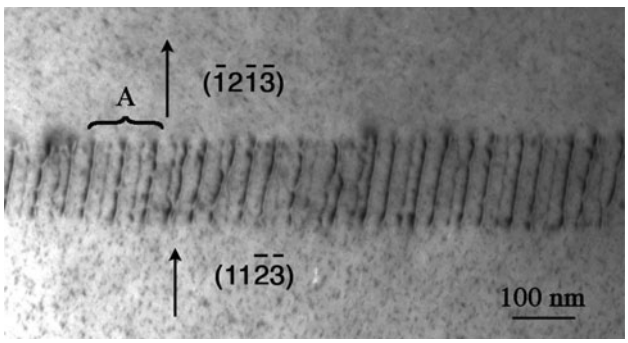

Fig. 3 Two-beams common **g** image of the rhombohedral twin in the as-received doped bicrystal. Disconnections with strong and weak contrast are alternately distributed in the part *A* of the GB. This arrangement corresponds to the equilibrium GB structure of the undoped bicrystal. The disconnections have Burgers vectors with opposite component along the axis $[2\bar{1}\bar{1}0]$. The doped bicrystal displays a much more complex structure, as evidenced in Fig. 4

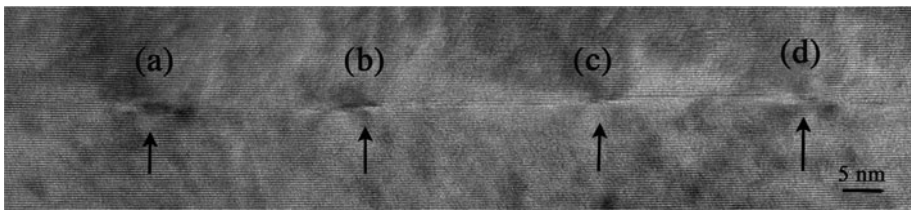

Fig. 4 Low magnification HRTEM image of four disconnections in the doped bicrystal. Disconnections **a** and **d** have descending steps, disconnections **b** and **c** ascending steps (see text)

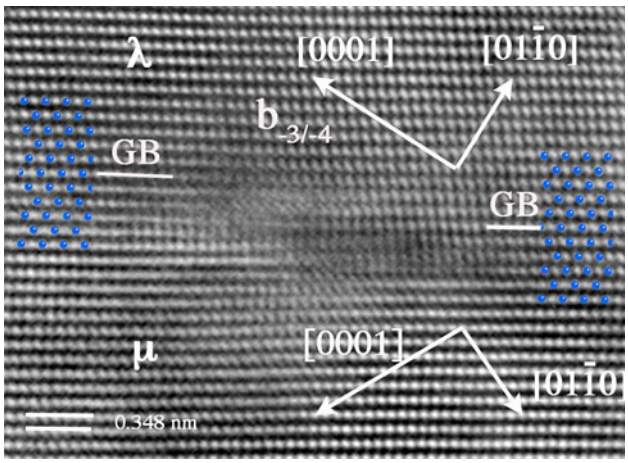

Fig. 5 HRTEM image of a $\vec{b}_{-3/-4}$ disconnection ((a) in Fig. 4) in the doped bicrystal along the zone axis $[2\bar{1}\bar{1}0]$ in the upper crystal λ. The GB plane is $(01\bar{1}2)_{\lambda}$ ($d = 348$ pm). The other dense plane is $(0\bar{1}14)_{\lambda}$ ($d = 255$ pm). The *white dots* correspond to empty sites of the structure. The alumina cell is centred on empty sites of the structure. Between these *white dots*, the *black* contrast corresponds to two aluminium columns and three oxygen columns. The models of the perfect twin structure are superimposed to the image; only lattice sites (in *blue*) appear in the model (Color figure online)

GB plane (length 348 pm = d $(01\bar{1}2)$), a component parallel to the zone axis $[2\bar{1}\bar{1}0]_{\lambda}$ (length 238 pm) and a small component parallel to $[01\bar{1}\bar{1}]_{\lambda}$ (length 70 pm for $\vec{b}_{-3/-4}$ disconnection). The disconnection core image is blurred. This can be a result of a slight inclination of the defect along the projection axis, or of a preferred irradiation of the core under the electron beam.

Other defects in Fig. 4 have the following Burgers vectors: (b) disconnection $\vec{b}_{2/1}$, (c) disconnection $\vec{b}_{3/2}$, (d) disconnection $\vec{b}_{-3/-4}$. It is recalled that the disconnections in the undoped bicrystal have the smallest Burgers vectors of the twin, namely, $\vec{b}_{-3/-4}$ and $\vec{b}_{-4/-5}$. Disconnections $\vec{b}_{2/1}$ and $\vec{b}_{3/2}$ should decompose into $\vec{b}_{4/3}$ and one or two $\vec{b}_{1/1}$ [41].

This local distribution of disconnections corresponds to an out of equilibrium structure compared to the situation in the undoped bicrystal, as close dislocations show similar screw component.

GB characteristics in the crept bicrystal

Main deformation features

The grains display evidence for basal slip deformation. Isolated basal dislocations, dipoles, and strings of loops are present after a deformation of 0.13% (Fig. 6). The dislocation density is higher near the GB than in the other parts of the thin foil, but no pile-ups occur.

The two basal slip systems have been activated in each crystal. In Fig. 6b, the curved dislocation **1** of Fig. 6a has a symmetrical contrast characteristic of $\vec{g} \cdot \vec{b} = 0$ in its straight parts. The curved part is out of contrast. Other dislocations 2 and 3 show a strong asymmetrical contrast. Mainly 60° dislocations are encountered. Figure 7 shows interactions between crystal dislocations and the GB.

The GB displays a fine periodic network of intrinsic dislocations. Extrinsic dislocations are also visible. A

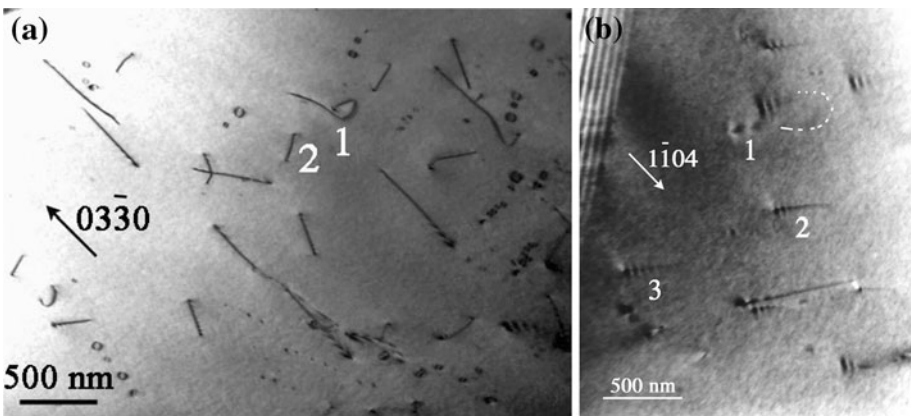

Fig. 6 Dislocations in the grains near the GB: **a** Bright field image showing basal dislocations and loops in the lower grain under the GB. **b** Dark field image (the contrast is reversed for better imaging of defects). Dislocation **1** is out of contrast in its curved part (along *dotted curve*) and has a symmetric contrast for straight parts. Dislocations **2** and **3** present a strong asymmetrical contrast

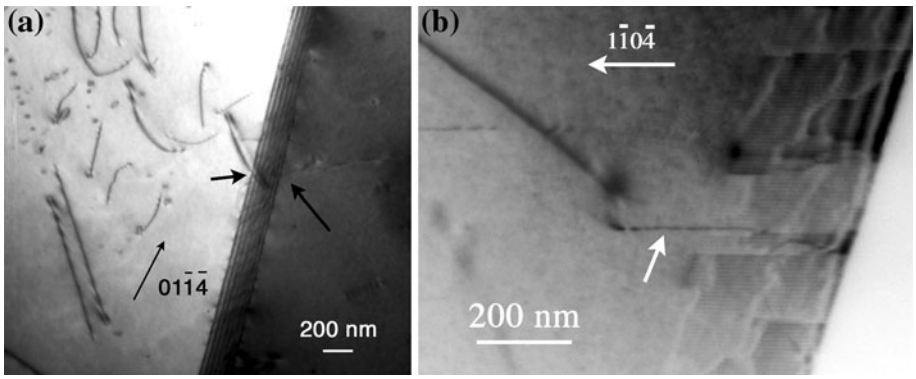

Fig. 7 **a** Bright field image, *left* crystal contains dislocation dipoles and strings of loops. Dislocations close to the GB are *arrowed*. b Dark field image (reversed contrast) showing an interaction between a lattice dislocation and the GB. The intrinsic disconnection network is visible, as well as extrinsic defects

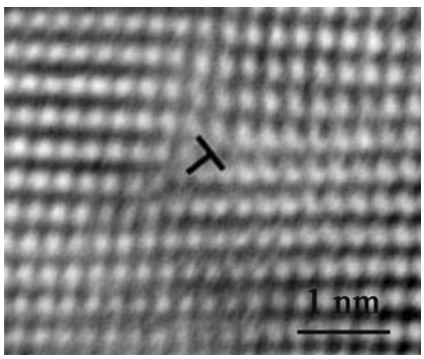

Fig. 8 HRTEM image of a lattice dislocation near the GB

lattice dislocation close to the GB is imaged in high resolution on Fig. 8. The dislocation does not appear to be dissociated, as expected for dislocations gliding in the basal slip. Basal dislocations undergo diffusion-controlled climb dissociation when their glide motion is stopped [43, 44]. Our result could arise from a decrease in cation diffusivity or an increase in stacking fault energy due to magnesium [27].

The HRTEM investigations on several thin foils reveal that most disconnections have a $b_{+1/-1}$ Burgers vector, perpendicular to the GB and with a large length of 696 pm. Numerous $\vec{b}_{0/-2}$ are also found. They form an almost perfect sub-boundary superimposed to the rhombohedral twin, and the mean distance between the disconnections is close to 9 nm, in agreement with the measured tilt deviation angle of 4.4°. The successive disconnections near and in the analysed area shown in Fig. 9 have the following Burgers vectors, reported in the dichromatic pattern of the twin Fig. 10:

$$\vec{b}_{0/-2}, \vec{b}_{+1/-1}, \vec{b}_{+1/-1}, \vec{b}_{+1/-1}, \vec{b}_{+1/-1},$$

$$\vec{b}_{-2/-5}, \vec{b}_{-1/-3}, \vec{b}_{0/-2}, \vec{b}_{+1/-1}, \vec{b}_{0/-2},$$

Shown in Fig. 9

$$\vec{b}_{0/-2}, \vec{b}_{+1/-1}, \vec{b}_{0/-2}, \vec{b}_{+1/-1}.$$

It is seen that the disconnections are dissociated (Fig. 11). The GB part between the two $(01\bar{1}2)$ inserted planes corresponds to a structure centred on oxygen ions, rather than on empty sites of the alumina structure. It is called S(O) in [39] and has a high energy. However, the disconnection energy should be decreased by dissociation. Due to the large Burgers vector length (696 pm), six anion planes are inserted and should terminate on a same $(01\bar{1}2)$ plane, a rather *unlikely* configuration. Dissociation here requires climb of the partials. It is worth noting that dissociation occurs in low angle GBs in alumina [45], and also for $\vec{b}_{-3/-4}$ and $\vec{b}_{-4/-5}$ in the rhombohedral twin [41].

GB disconnection interactions with lattice dislocations

It is assumed that the two crystals are deformed symmetrically with the GB. The situation is schematically represented in Fig. 2. In that case, the specimen compression originates from one dislocation in each grain moving

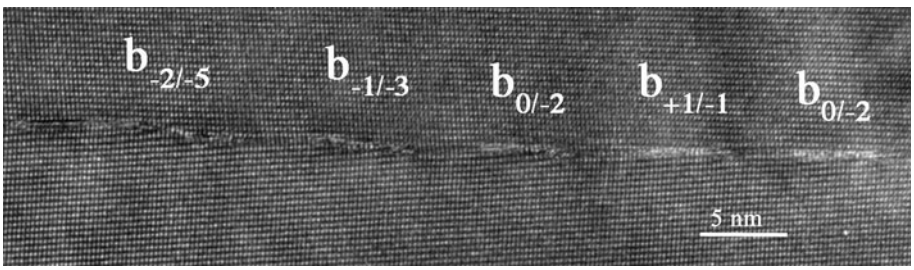

Fig. 9 HRTEM image of the deformed bicrystal after creep deformation showing five disconnections with various Burgers vectors

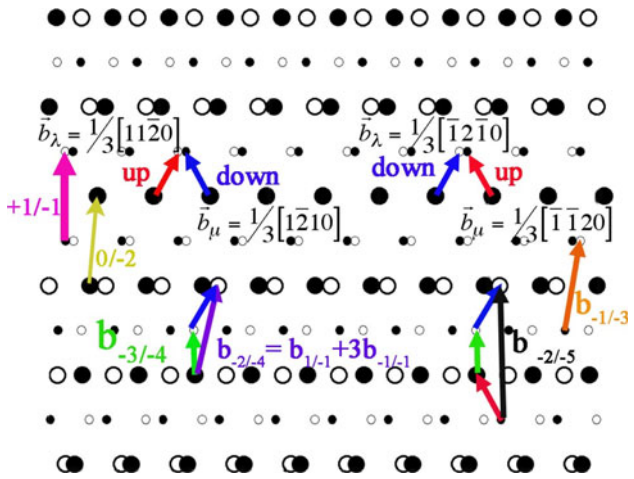

Fig. 10 Dichromatic pattern of the rhombohedral twin. The symbols correspond to lattice sites. *White symbols* correspond to the crystal λ, *black symbols* to the crystal μ. *Small symbols* correspond to positions at $z = 1/2$. Disconnection Burgers vectors of Fig. 9 are reported. The couple of possible dislocations Burgers vectors according to the symmetrical glide in the bicrystal are figured in the top of the pattern. The reaction between $\vec{b}_{-3/-4}$ and $\vec{b}_\lambda = \frac{1}{3}[\bar{1}2\bar{1}0]$ leads to a $\vec{b}_{-2/-4}$ Burgers vector, which decomposes into glissile dislocations and a $b_{+1/-1}$ dislocation (see text). The observed $\vec{b}_{-2/-5}$ results from the interaction of a $\vec{b}_{-3/-4}$ with two perfect dislocations from the λ and μ crystals (See GB disconnection interactions with lattice dislocations)

towards the GB. In the other case, one dislocation moves across the GB. In both cases, the final homogeneous deformation of the bicrystal leads to a wall edge dislocations added to the initial GB [46] (Fig. 2b). The situation is complicated by the fact that two slip systems are activated. The two sets of dislocations for both configurations are the following (Fig. 10):

$$\vec{b}_\lambda = \frac{1}{3}[11\bar{2}0]_{(\mathrm{up})},\ \vec{b}_\mu = \frac{1}{3}[1\bar{2}10]_{(\mathrm{down})}$$

$$\vec{b}_\lambda = \frac{1}{3}[\bar{1}2\bar{1}0]_{(\mathrm{down})},\ \vec{b}_\mu = \frac{1}{3}[\bar{1}\bar{1}20]_{(\mathrm{up})}.$$

The characters "up" and "down" correspond to the sense of the Burgers vectors along the axis $[2\bar{1}\bar{1}0]_\lambda$.

The sum of the two lattice vectors $\vec{b}_\lambda$ and $\vec{b}_\mu$ gives the $\vec{b}_{+1/-1}$ GB vector.4

The possible mechanisms of interaction are as follows:

Interaction of a lattice dislocation and a GB disconnection The example of the reaction between $\vec{b}_{-3/-4}$ and $\vec{b}_\lambda = \frac{1}{3}[\bar{1}2\bar{1}0]$ is analysed. On the dichromatic pattern of Fig. 10, the reaction leads to a $\vec{b}_{-2/-4}$ Burgers vector that may decompose into a $\vec{b}_{0/-2}$ (observed) and two $\vec{b}_{-1/-1}$ that are glissile (shear vector of the twin, length 70 pm). The $\vec{b}_{0/-2}$ may then decompose into $\vec{b}_{+1/-1}$ and $\vec{b}_{-1/-1}$ Burgers vectors. The case of the formation of the $\vec{b}_{-2/-5}$ is interesting, as it results from the reaction between a $\vec{b}_{-3/-4}$ and 2 dislocations in each crystal. This implies that the two slip systems correspond in the two grains and consequently dislocations of one and the other grain arrive in the same area of the GB, as already observed in other materials [28].

Decomposition of a lattice dislocation into GB disconnections Possible decomposition of lattice dislocations in GB disconnections are shown in Fig. 12: For example, $\vec{b}_\mu = \frac{1}{3}[1\bar{2}10]$ decomposes into $\vec{b}_{-3/-4}$ and three $-\vec{b}_{-1/-1}$ disconnections. The products $\vec{b}_{-1/-1}$ and $\vec{b}_{1/1}$are glissile

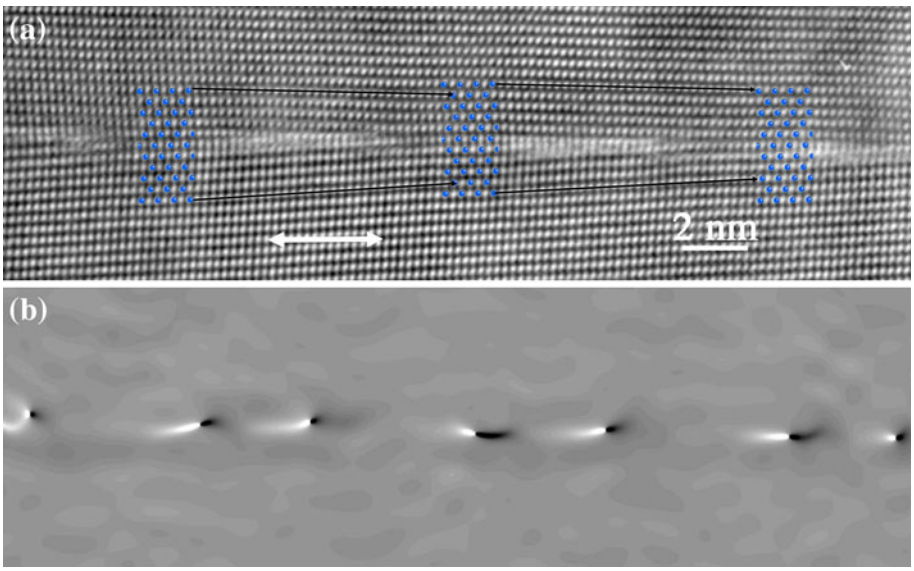

Fig. 11 **a** HRTEM image of two disconnections i ($\vec{b}_{+1/-1}$) and j ($\vec{b}_{0/-2}$). In the structural models, *blue dots* correspond to empty sites of alumina. **b** geometrical phase: Local y component of $\vec{g}(01\bar{1}2)$ showing a dissociation width of 2–3 nm (Color figure online)

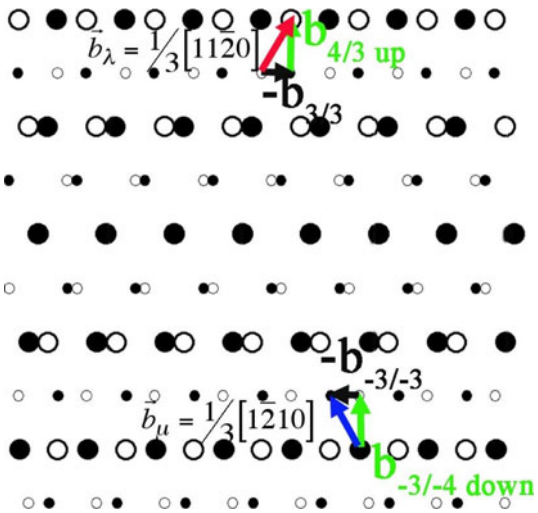

Fig. 12 Possible decompositions of perfect lattice dislocations (*blue* and *red*) into glissile disconnections and $\vec{b}_{4/3}$ or $\vec{b}_{-3/-4}$ disconnections (*light grey*, *green*) (Color figure online)

and can annihilate. The Burgers vectors $\vec{b}_{-3/-4}$ and $\vec{b}_{4/3}$ are chosen because they are the smallest Burgers vectors of the twin with a component out of the GB plane. Their screw components have opposite signs. They may interact by climb, the result of the interaction is $\vec{b}_{+1/-1}$.

A transmission of glide through the GB is unlikely, the $\vec{b}_{+1/-1}$ being very large. Moreover, it requires very high stresses to operate [47, 48]. An indirect transmission, implying absorption of lattice dislocations from one crystal followed by reaction within the GB and emission of lattice dislocations in the other crystal could occur. The transmission process efficiency depends on the mobility of GB disconnections. However, the presence of numerous dislocations in both grains close to the GB shows that the GB merely plays a role of obstacle for incoming dislocations.

If the bicrystal orientation was such that slip in one crystal is favoured, the number of glissile disconnections in one sense should be higher and promote GB sliding. In zinc, sliding is promoted by the interaction of lattice dislocations with the GB [18]. Sliding behaviour analysed at a mesoscopic scale is interpreted by the decomposition of lattice dislocations into sessile dislocations with zero step height and glissile dislocations with a minimal step height [19]. These processes depend on GB chemistry. Then, the next objective will be to investigate the effect of GB segregation on interaction mechanisms between lattice dislocations and GBs.

Conclusion

Two basal slip systems are activated during creep of bicrystals near the rhombohedral twin orientation. Basal dislocations interact with the GB leading to an increase in the deviation angle by 3.6°. The GB disconnection structure changes from an arrangement of two parallel arrays of disconnections with the smallest Burgers vectors but large associated steps to a parallel array of pure edge disconnections with a large Burgers vector without step. These defects appear always dissociated. They can result from reactions with GB disconnection or decomposition reactions of lattice dislocations within the GBs. In both cases, glissile disconnections eliminate themselves due to the symmetric orientation of the bicrystal with respect to slip systems in both crystals.

Acknowledgments E. A. Stepantsov and A. L. Vasiliev from the Institute of Crystallography of Moscow are gratefully acknowledged for the preparation of the bicrystals.

References

1. Lartigue S, Priester L (1988) J Am Ceram Soc 71:430
2. Lartigue-Korinek S, Dupau F (1994) Acta Metall Mater 42:293
3. Pond RC, Smith DA, Southerdern PWJ (1978) Philos Mag A37:27
4. Valiev RZ, Gertsman VY, Kaibystshev OA (1983) Phys Stat Sol A77:97
5. Cho J, Harmer MP, Chan H, Rickman JM, Thompson AM (1997) J Am Ceram Soc 80:1013
6. Yoshida H, Ikuhara Y, Sakuma T (2002) Acta Mater 50:2955
7. Lartigue-Korinek S, Carry C, Priester L (2002) J Eur Ceram Soc 22:1525
8. Bouchet D, Lartigue Korinek S, Molins R, Thibault J (2006) Philos Mag 86:1401
9. Monzen R, Sumi Y, Kitagawa K, Mori T (1990) Acta Metall Mater 38:2553
10. Hanyu S, Nishimura H, Matsunaga K, Yamamoto T, Ikuhara Y, Sakuma T (2004) Mater Trans 45:2122
11. Matsunaga K, Nishimura H, Muto H, Yamamoto T, Ikuhara Y (2003) Appl Phys Lett 82:1179
12. Yoshida H, Ikuhara Y, Sakuma T (1999) Philos Mag Lett 79:249
13. Nakamura K, Mizogushi T, Shibata N, Matsunaga K, Yamamoto T, Ikuhara Y (2007) Phys Rev B 75:184109
14. Milas I, Carter EA (2009) J Mater Sci 44:1741. doi: 10.1007/s10853-008-3191-z
15. Kegg GR, Horton CAP, Silcock JM (1973) Philos Mag A 27:1041
16. Gleiter H (1981) Prog Mater Sci 25:125
17. Kokawa H, Watanabe T, Karashima S (1981) Philos Mag A 44:1239
18. Valiev RZ, Kaibyshev OA, Astanin VV, Emaletdinov AK (1983) Phys Stat Sol 78:439
19. Sheikh-Ali AD, Lavrentyev FF, Kazarov YuG (1997) Acta Mater 45:4505
20. Yoshida H, Yokoyama K, Shibata N, Ikuhara Y, Sakuma T (2004) Acta Mater 52:2349
21. Miller L, Avishai A, Kaplan WD (2006) J Am Ceram Soc 89:350
22. Soni KK, Thompson AM, Harmer MP, Williams DB, Vhabala JM, Levi-Setti R (1995) Appl PhysLett 66:2795
23. Gavrilov KL, Bennison SJ, Mikeska KR, Chabala JM, Levi-Setti R (1999) J Am Ceram Soc 82:1001
24. Sakagushi I, Srikanth V, Ikegami T, Haneda H (1995) J Am Ceram Soc 78:2557
25. Snow JP, Heuer AH (1973) J Am Ceram Soc 56(3):153

26. Pletka BJ, Mitchell TE, Heuer AH (1974) J Am Ceram Soc 57(9):388
27. Pletka BJ, Mitchell TE, Heuer AH (1982) Acta Metall 30:147
28. Lagerlöf KPD, Heuer AH, Castaing J, Rivière JP, Mitchell TE (1994) J Am Ceram Soc 77(2):385
29. Castillo Rodriguez M, Castaing J, Munoz A, Veyssières P, Dominguez Rodriguez A (2008) J Am Ceram Soc 91(5):1612
30. Scott WD, Orr KK (1975) Deformation of ceramic materials. Plenum, New York, p 151
31. Castaing J, Munoz A, Gomez Garcia D, Dominguez Rodriguez A (1997) Mater Sci Eng A233:121
32. Vasiliev AL, Stepantsov EA, Ivanov ZG, Verbist K, Van Tendeloo G, Olsson E (1997) Appl Surf Sci 119:215
33. Pond RC (1989) In: Nabarro FRN (ed) Dislocations in Solids, vol 8. Elsevier Science Publishers, Amsterdam, p 1
34. website http://www.totalresolution.com
35. Marukawa K, Matsubara Y (1979) Trans JIM 20:560
36. Geipel T, Lagerlöf KPD, Pirouz P, Heuer AH (1994) Acta Mater 42:1367
37. Lartigue-Korinek S, Hagege S (1999) In: Lejcek P, Paidar V (eds) Materials Science Forum, vols 294–296. Trans Tech Publications, Switzerland, p 281
38. Gemming T, Nufer S, Kurtz W, Ruehle M (2003) J Am Ceram Soc 86:581
39. Marinopoulos AG, Elsässer C (2000) Acta Mater 48:4375
40. Nishimura H, Matsunaga K, Saito T, Yamamoto T, Ikuhara Y (2003) J Am Ceram Soc 86:574
41. Lartigue-Korinek S, Hagège S, Kisielowski C, Serra A (2008) Philos Mag 881:569
42. Braisaz T, Ruterana P, Nouet G, Pond RC (1997) Philos Mag A 75:1075
43. Mitchell TE, Pletka BJ, Phillips DS, Heuer AH (1976) Philos Mag 34:441
44. Nakamura A, Yamamoto T, Ikuhara Y (2002) Acta Mater 50:101
45. Nakamura A, Matsunaga K, Yamamoto T, Ikuhara Y (2006) Philos Mag 86:4657
46. Bacmann JJ, Gay MO, De Tournemine R (1982) Scr Metall 16:353
47. Thibault J, Putaux JL, Jacques A, George A, Elkajbaji M (1990) Microsc Microanal Microstruct 1:395
48. Priester L (2001) Mater Sci Eng A 309–310:430